



Article

Electronic and Structural Properties of Antibacterial Ag–Ti-Based Surfaces: An Ab Initio Theoretical Study

Stefanos Papantoniou-Chatzigiosis¹, Athina C. Galani¹, Dimitra Fylaktopoylou¹, Christina Kourti¹, Androniki Mosxou¹, Maria E. Nousia^{1,2} , Thomas Anthopoulos^{3,4}, Elefterios Lidorikis¹  and Christina E. Lekka^{1,*}

- ¹ Department of Materials Science and Engineering, University of Ioannina, 45110 Ioannina, Greece; stefanospap09@gmail.com (S.P.-C.); galaniath@hotmail.com (A.C.G.); fylaktopoulou@gmail.com (D.F.); stm01755@uoi.gr (C.K.); andronikimoschou@gmail.com (A.M.); mariaevanthia.nousia@unito.it (M.E.N.); elidorik@uoi.gr (E.L.)
- ² Department of Chemistry, University of Torino, 10124 Torino, Italy
- ³ PSE Division, King Abdullah University of Science and Technology (KAUST), Jidda 23955-6900, Saudi Arabia; thomas.anthopoulos@manchester.ac.uk
- ⁴ Henry Royce Institute, Photon Science Institute, Department of Electrical and Electronic Engineering, The University of Manchester, Manchester M13 9PL, UK
- * Correspondence: chlekka@uoi.gr

Abstract: Coatings with tunable multifunctional features are important for several technological applications. Ti-based materials have been used in diverse applications ranging from metallic diodes in electronic devices up to medical implants. This work uses ab initio calculations to achieve a more fundamental understanding of the structural and electronic properties of β -TiNb and its passive TiO₂ film surfaces upon Ag addition, investigating the alterations in the electronic band gap and the stability of the antibacterial coating. We find that Ag's 4d electrons introduce localized electron states, characterized by bonding features with the favoured Ti first neighbour atoms, approximately -5 eV below the Fermi level in both β -TiNb bulk and surface. Ag's binding energy on β -TiNb(110) depends on the local environment (the lattice site and the type of bonded surface atoms) ranging from -2.70 eV up to -4.21 eV for the adatom on a four-fold Ti site, offering a variety of options for the design of a stable coating or for Ag ion release. In Ti–O terminated anatase and rutile (001) surfaces, surface states are introduced altering the TiO₂ band gap. Silver is bonded more strongly, and therefore creates a more stable antibacterial coat on rutile than on anatase. In addition, the Ag coating exhibits enhanced 4d electron states at the highest occupied state on anatase (001), which are extended from -5 eV up to the Fermi level on rutile (001), which might be altered depending on the coat structural features, thus creating systems with tunable electronic band gap that can be used for the design of thin film semiconductors.

Keywords: biocompatible coatings; metallic–semiconductor interfaces; DFT



Citation: Papantoniou-Chatzigiosis, S.; Galani, A.C.; Fylaktopoylou, D.; Kourti, C.; Mosxou, A.; Nousia, M.E.; Anthopoulos, T.; Lidorikis, E.; Lekka, C.E. Electronic and Structural Properties of Antibacterial Ag–Ti-Based Surfaces: An Ab Initio Theoretical Study. *Crystals* **2024**, *14*, 428. <https://doi.org/10.3390/cryst14050428>

Academic Editor: Dejun Li

Received: 28 March 2024

Revised: 13 April 2024

Accepted: 14 April 2024

Published: 30 April 2024



Copyright: © 2024 by the authors. Licensee MDPI, Basel, Switzerland. This article is an open access article distributed under the terms and conditions of the Creative Commons Attribution (CC BY) license (<https://creativecommons.org/licenses/by/4.0/>).

1. Introduction

Titanium-based biocompatible surfaces are critical in tissue engineering, osteogenesis and bacterial adhesion, as well as in implantable organic and smart electronics devices [1–12]. With the aim to include antimicrobial properties in non-biodegradable implants, selective molecular or polymeric coatings along with antibacterial elements have been used for the manufacturing of medical device surfaces [13–18]. Anticancer L-glutamine green corrosion inhibitor is bonded on antibacterial Cu (111) suitable for coating on Ti-based implants [13], while antibacterial polyurethanes exhibit appropriate mechanical properties and hemocompatibility [14]. Silver complexes with natural extracts have been successfully used to create contact lens hydrogels with anti-microbial properties [15], while the bactericidal activity of silver nanoparticles along with their advantages and disadvantages

for cell environment toxicity have also been extensively studied [16]. In addition, doping with other antibacterial elements such as Ga or Cu and oxides has been successfully applied to β -Ti-based alloys revealing antimicrobial ability, and improving bone repair and angiogenesis [19–23]. Ga antibacterial inclusions in β -TiNb result in a stable solid solution with increased strength and Young's modulus due to the new Ga–Ti super sp-like bonding orbitals along specific directions [21]. Furthermore, the inclusion of Ag in the FeMn biodegradable implant induces martensitic transformation due to the creation of local depletion of the electronic charge at the intrinsic stacking fault plane, thus weakening the atomic bonds and gradually increasing the magnetization of the material, creating a material with tunable physical properties suitable for several technological applications [24,25].

Ag nanoparticles in 3D or 2D coating applied on the TiO_2 that is naturally formed on Ti-based surfaces enhance the antibacterial activity [26–32]. In addition, the alterations in the titanium oxide semiconductor band gap reveal a material suitable for several technological applications beyond biomedical, such as photocatalysis and solar cells [26,31,32]. Specifically, the semiconductor Ti–O passive layer formed on metallic diodes has a tunable bandgap, rendering this material interesting for multifunctional applications such as thin-film transistors and electronic devices [9–12,26,31,32]. The creation of new electron states and charge transfer at the metal–semiconductor interface or on the oxide surface can be further tuned upon Ag doping, giving interesting opportunities for electronic and optoelectronic applications [26–32].

Nevertheless, to our knowledge, the theoretical investigation of the early-stage growth of Ag on Ti-based surfaces is limited. Single metal atoms' binding energies and adsorption sites on oxides have been reported by density functional theory studies, exhibiting a weaker Ag adatom bonding to the oxide surfaces compared to other metals such as V [33–35]. This is interesting, since Ag's biocompatibility is related to the positive silver ions that are released from the surface during exposure to the human body, carrying antibacterial activity (they are strongly bactericidal) and limiting not only infections but also the formation of biofilms on the surface of the implant [30].

In this work, a fundamental understanding of the structural and electronic properties of Ag addition to β -Ti-based alloys is performed by DFT calculations. First, Ag in β -TiNb will be considered, then Ag adatom, followed by half and full 2D coating on β -TiNb surfaces. Since Ti surfaces are easily oxidized it is critical not only to investigate Ag adsorption on the metallic β -TiNb surfaces but also to understand Ag's behavior on the TiO_2 that is usually observed experimentally. Therefore, the alterations in structural and electronic properties due to the presence of an oxide passive layer will be investigated for both anatase and rutile structures along with the electronic origin of the TiO_2 semiconductor band gap alterations. These results could be used for the design of metal-oxide coatings for multifunctional applications, starting from bone implants to electronic devices.

2. Computational Details

Density functional theory calculations are used by means of the VASP code for the oxides [36,37] and the SIESTA code for metals and oxides [38,39], along with the PBE (Perdew–Burke–Ernzerhof) generalized gradient-corrected approximation [40]. In VASP, the projector augmented wave (PAW) potentials were generated by G. Kresse [41] whereas the PAW method was first suggested and used by Peter Blöchl [42]. A plane wave basis set is adopted with 400 eV (250 eV) planewave energy cutoff for the oxide cases (for β -TiNbAg cases without oxygen) which includes the valence electrons for all elements along with the 3p and 4p of Ti and Nb semicore orbitals respectively. In SIESTA, core and semicore electrons are replaced by norm-conserving pseudopotentials in the fully nonlocal Kleinman–Bylander form, while the basis set is a linear combination of numerical atomic orbitals (NAOs) constructed from the eigenstates of the atomic pseudopotentials [38,39]. It should be noted that for small organic molecules and metallic atoms on surfaces or tiny clusters, there are dispersion corrections, such as PBE+D3 in the DFT calculations to better describe the long-range interactions providing better adsorption energies and

activation barriers [43–45]. In addition, hybrid (M06) or metahybrid PBE+D3/M06 functionals developed for highly correlated systems also provide a reasonable description of noncovalent interactions [45]. It should be noted that in this work, the choice of a PBE+D3 or PBE+D3/M06 functional including long-range interactions, van der Waals forces and hybrid functions could indeed lower the Ag adatom binding energy on β -TiNb(110), but it would affect the 2D periodic Ag (half/full) monolayer on surfaces or the 3D bulk systems less. Furthermore, in SIESTA calculations the double- ζ polarization (DZP) basis sets to describe the valence and if needed DZP or single- ζ semicore states of the species were used with the standard orbital-confining cutoff radii. The NAOs are confined, being strictly zero beyond a certain radius. In particular, for every Ti atom double ζ basis with 26 NAOs was used: two 3s (rc = 2.743 Bohr, 2.083 Bohr) and 4s (rc = 6.258 Bohr, 5.732 Bohr) shells, six 3p (rc = 3.031 Bohr, 2.057 Bohr) and 4p (rc = 7.092 Bohr, 6.028 Bohr) shells and 10 3d (rc = 4.301 Bohr, 2.675 Bohr) shells (in parentheses the 1st and 2nd ζ cut off radius are depicted for the β -TiNbAg while tiny radius modifications of the 1st ζ is observed for the other cases). For the Nb atom we used 19 NAOs with single ζ for the semi core 4s (rc = 2.964 Bohr) and three 4p (rc = 3.358 Bohr), double ζ for the valence two 5s (rc = 6.934 Bohr, 6.679 Bohr) and ten 4d (rc = 5.400 Bohr, 3.620 Bohr) along with three 5p (rc = 8.469 Bohr) shells. For the Ag atom NAOs were used: double ζ for the valence two 5s (rc = 6.854 Bohr, 6.359 Bohr) and ten 4d (rc = 4.157 Bohr, 2.521 Bohr) along with three single ζ 5p (rc = 10.225 Bohr). For the O atom we used 13 NAOs double ζ for the two 2s (rc = 3.937 Bohr, 2.574 Bohr), six 2p and five polarized 2P (rc = 4.931 Bohr, 2.672 Bohr) shells, respectively. An auxiliary real space grid equivalent to a plane-wave cut-off of 200 Ry was used. The self-consistency is achieved when the change in the total energy between cycles of the SCF procedure is below 10^{-4} eV (energy convergence criterion), and the density matrix change criterion 10^{-4} is also satisfied. The Ti and Nb pseudo-potentials and basis sets were tested in authors previous work [46] and found to successfully reproduce the basic structural and electronic features of the monoatomic β -Ti and β -Nb and the TiNb CsCl phase with space group Im-3m defined by one atom located at the origin and another at the middle of the unit cell.

The presence of Ag in β -TiNb and TiO₂ was simulated with several supercells and sampling of the Brillouin zone using appropriate periodic boundary conditions.

Section 3.1. Ag in β -TiNb:

Ag in bulk β -TiNb: In Section 3.1, for the Ti₆₈Nb₃₀Ag₂ (atomic units at%) alloy a $3 \times 3 \times 3$ supercell ($9.831 \text{ \AA} \times 9.831 \text{ \AA} \times 9.831 \text{ \AA}$ for the calculated 3.277 \AA lattice constant) was considered and a $5 \times 5 \times 5$ k-point sampling was employed by applying periodic boundary condition in the three dimensions (3D) to mimic the bulk system while by reordering the Ti and Nb atoms, a different first neighborhood was achieved for Ag atoms in line with previous calculations [6,21,47].

Section 3.2. Adsorption of Ag on β -TiNb surface:

(3.2.a) Ordered β -TiNb(001) and β -TiNb(110) surfaces: In Section 3.2, the β -TiNb(001) and β -TiNb(110) were created by considering $1 \times 1 \times 10$ unit cells along the corresponding [001] and [110] directions, thus creating 20 atomic planes with two atoms, while a $20 \times 20 \times 1$ k-point mesh was applied only in-plane along with two-dimension (2D) periodic boundary conditions to mimic the infinite surface. In the [001] or [110] directions, the size of the imaginary box chosen was 2.5 times larger than the length of the 20 atomic planes in order to apply periodic boundary conditions vertically to the surface plane (avoiding the interactions between the upper and bottom surface planes). In addition, the supercell's middle (10th) atomic layer's relative relax position was found to be 0.1% compared to the perfect bulk interatomic distance, suggesting an appropriate description of the bulk β -TiNb distance in the central atomic layers of the system with surfaces.

(3.2.b) Ag on ordered β -TiNb(110) surface: Upon Ag adsorption on the perfect ordered β -TiNb(110), two cases were considered: (a) Ag full 2D coating on the $1 \times 1 \times 10$ β -TiNb(110) supercell using 2 Ag atoms and (b) Ag "half" 2D coating on the $1 \times 1 \times 10$ β -TiNb(110)

supercell using 1 Ag in different sites along with in-plane 2D periodic boundary conditions. A $20 \times 20 \times 1$ k-point mesh was applied only to the in-plane directions. The inplane supercell size was $4.634 \text{ \AA} \times 3.277 \text{ \AA}$ while along the [110] direction the size was 46.340 \AA (of the β -TiNb(110)) plus the Ag coating area that was relaxed from 2.795 \AA to 2.913 \AA for the different cases as presented in the corresponding figure of Section 3.2.

(3.2.c) Disorder β -TiNb(110) surface layer: Aiming to approach the β -TiNb solid solution surface (where the Ti and Nb do not occupy the perfect and ordered unit cell positions), a $3 \times 3 \times 3$ supercell of the four-atom β -TiNb(110) unit cell was created resulting in six atomic planes with eighteen atoms each (Supercell dimensions $13.902 \text{ \AA} \times 9.831 \text{ \AA} \times 13.902 \text{ \AA}$). Thus, the surface layer had 9Ti and 9Nb surface atoms that were rearranged in order to approach several disorder cases, as presented in Section 3.2. To mimic the bulk system, the three bottom atomic layers were frozen.

(3.2.d) Ag adatom on the disordered β -TiNb(110) case: Only one Ag atom was deposited on different sites on the favoured disorder β -TiNb(110) surface, and in-plane periodic boundary conditions were employed. The system was large in order to limit adatom–adatom interactions of the periodic images. The supercell dimensions are the ones of the disorder β -TiNb(110) surface layer $13.902 \text{ \AA} \times 9.831 \text{ \AA} \times 13.902 \text{ \AA}$ plus the Ag adatom at 2.701 \AA resulting a supercell of $13.902 \text{ \AA} \times 9.831 \text{ \AA} \times 16.603 \text{ \AA}$ that was inside a imaginary box of $13.902 \text{ \AA} \times 9.831 \text{ \AA} \times 100 \text{ \AA}$.

Section 3.3. Ag adsorption on anatase and rutile TiO_2 surfaces:

Ag coating on TiO_2 (001) surfaces: The adsorption of Ag atoms on the anatase or rutile oxide surface is performed either on the Ti surface atoms (OnTop sites) or the Ti second layer atoms (Four Fold sites) named as half coverage while the Ag adsorption over all available site results the full coverage. In -plane periodic boundary conditions were applied along with $10 \times 10 \times 1$ kpoint meshes.

Supporting Information. Anatase and Rutile TiO_2 and TiO_2 (001) surfaces

(S.I.a) TiO_2 Anatase and Rutile bulk oxides: For the calculation of the total energy curves the unit cells of TiO_2 rutile ($4.614 \text{ \AA} \times 4.614 \text{ \AA} \times 2.97 \text{ \AA}$) with $5 \times 5 \times 8$ k-points and anatase ($3.78 \text{ \AA} \times 3.78 \text{ \AA} \times 9.64 \text{ \AA}$) with $6 \times 6 \times 2$ k-points for the total energy curves with periodic boundary conditions in the three dimensions.

(S.I.b) TiO_2 Anatase and Rutile (001) surfaces: Aiming to calculate the anatase (001) and rutile (001) surfaces two supercells were considered. Due to the structure of the TiO_2 unit cell for the rutile $1 \times 1 \times 10$ units ($4.614 \text{ \AA} \times 4.614 \text{ \AA} \times 29.7 \text{ \AA}$) were considered while for anatase $1 \times 1 \times 4$ corresponding unit cells ($3.78 \text{ \AA} \times 3.78 \text{ \AA} \times 38.56 \text{ \AA}$). For both cases a $10 \times 10 \times 1$ k-point mesh was considered along with in-plane periodic boundary conditions. The size of the imaginary box was large enough along the z direction without vertical to the surface periodic boundary conditions.

For all cases, total energy minimization was performed until the forces within the atoms were smaller than 0.04 eV/\AA .

3. Results and Discussion

3.1. Ag in β -TiNb

The prototypical β -TiNb system we assume is $\text{Ti}_{70}\text{Nb}_{30}$ [6,21,47]. Aiming to reveal the energetically favoured Ag sites inside it, we consider $\text{Ti}_{68}\text{Nb}_{30}\text{Ag}_2$ (at%) $3 \times 3 \times 3$ supercells (i.e., close to 30 (at%) Nb composition) where the β solid solution phase is stable [6]. One Ag atom substitutes a Ti atom in different first neighbour environments, resulting in the composition $\text{Ti}_{68}\text{Nb}_{30}\text{Ag}_2$ (at%) in line with previous calculations of Ga, In, Sn and Hf in β -TiNb [6,21,47]. The available first neighbour environments (FN) offer Ag the opportunity to have Ti, Nb or TiNb in the first neighbourhood (named Ti_FN, Nb_FN and TiNb_FN). Ag prefers Ti_FN showing a total energy difference of -4.80 eV against -4.29 eV of the mix TiNb_FN and 3.00 eV of Nb_FN systems in line with previous calculations of Ga, In, Sn and Hf in β -TiNb [6,21,47]. Concerning the mechanical properties, the bulk

modulus of $\text{Ti}_{68}\text{Nb}_{30}\text{Ag}_2$ (at%), 135 GPa, is higher than the $\text{Ti}_{68}\text{Nb}_{30}\text{Ga}_2$ (at%) of 120 GPa and $\beta\text{-Ti}_{70}\text{Nb}_{30}$ (at%) of 130 GPa [21,46]. This is another advantage of Ag, since implant materials should be hard and bulk modulus is related to hardness [48].

The $\beta\text{-TiNbAg}$ electronic density of states (EDOS) is presented in Figure 1a. The inclusion of Ag in $\beta\text{-TiNb}$ exhibits a new broad energy state around -6 eV from the Fermi level compared to the pure $\beta\text{-TiNb}$ as can be seen in the total electronic density of states (EDOS) (Figure 1a). This electron energy state is mainly due to Ag 4d electrons, while at -5.5 eV it shows Ag 4d–Ti 3d hybridizations along the $[110]$ and $[-110]$ crystal directions (Figure 1b). The electron occupation close to the Fermi level is mainly due to Ti and Nb atoms that are mainly responsible for the metallic character of the material. In addition, the lowest valence electron state at -6.2 eV has clearly a Ag 5s character and an antibonding character with respect to the Ti neighbouring atoms, as presented in the (001) WF projection in the inset of Figure 1a. The presence of bonding and antibonding states at energies far from the Fermi level introduces system instability [6,21,46,47,49].

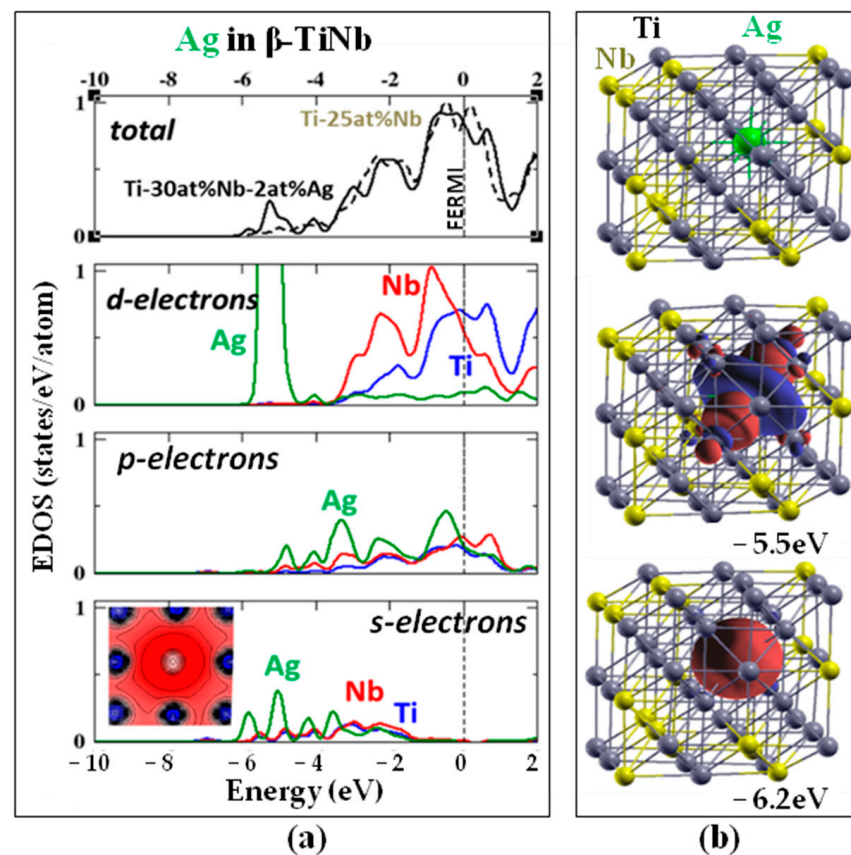


Figure 1. Ag in $\beta\text{-TiNb}$: (a) Total and partial electronic density of states and (b) characteristic wavefunctions. The total EDOSs of $\text{TiNb}_{30}\text{Ag}_2$ (at%) and TiNb_{25} (at%) are presented in black and dashed black lines, respectively. Ti, Nb and Ag partial EDOSs are shown in blue, red and green lines, respectively. Fermi energy is at 0 eV. Grey, yellow and green spheres stand for Ti, Nb and Ag atoms. Red and blue charge areas stand for the positive and negative sign of the wavefunction (from -0.1 up to $+0.1$ electrons/ \AA^3).

3.2. Adsorption of Ag on $\beta\text{-TiNb}$ Surface

The interaction of implants with biological tissues occurs through their surfaces, therefore working on the $\beta\text{-TiNb}$ surfaces is of particular importance. We started from the surfaces with the simplest geometry and structure that characterize the bcc crystal, i.e., with the low-index surfaces (001) and (110) . It is worth noting that bcc materials, especially Nb, prefer the (110) structure, which we expect for $\beta\text{-TiNb}$ [50].

We first created two surface-oriented unit cells along the (001) and (110) directions. In Figure 2a, the β -TiNb along the (110) is presented. We repeated these unit cells 10 times along the (001) or (110) directions, thus creating a slab with 20 atomic planes. During the DFT calculation, we increased the simulation length perpendicular to the surface plane to be at least twice the slab length while we periodically reproduced the in-plane direction to mimic the infinite plane. We also used a $20 \times 20 \times 1$ k-point mesh, as depicted in the blue arrow of Figure 2a.

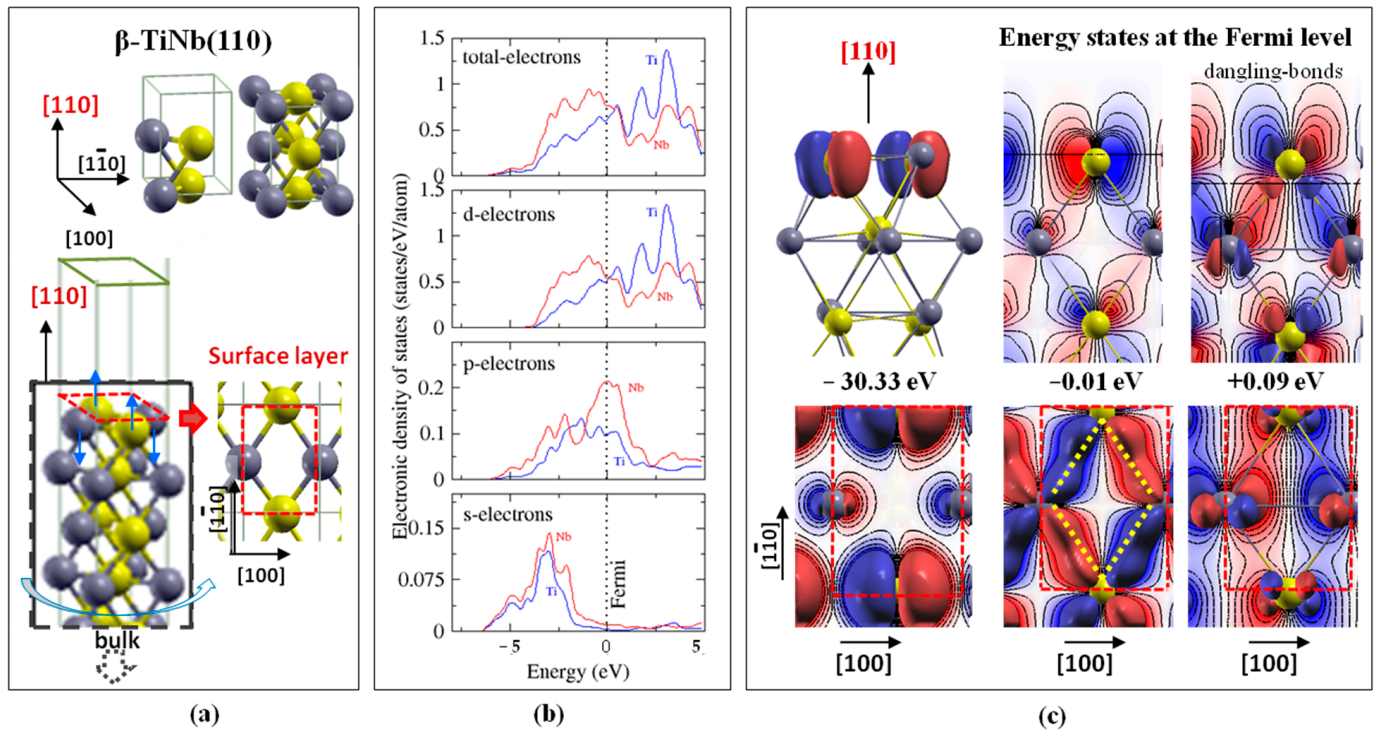


Figure 2. β -TiNb(110) surface: (a) Schematic representation of the surface unit cell, (b) total and partial electronic density of states and (c) characteristics wavefunctions. Fermi energy is at 0 eV. Blue arrows denote the Ti (Nb) surface atoms' expansion (contraction). Grey and yellow stand for Ti and Nb atoms. Red and blue charge areas stand for the positive and negative sign of the wavefunction (from -0.1 up to $+0.1$ electrons/ \AA^3).

The β -TiNb(001) crystal consists of Ti or Nb successive atomic planes, named here in β -TiNb(001)_Ti and β -TiNb(001)_Nb, while the β -TiNb(110) has a mix of Ti–Nb planes. Thus, for the β -TiNb(001) we studied two cases: Ti-terminated and Nb-terminated surface. The β -TiNb(110), shown in Figure 2a, has basis vectors $\vec{a}_1 = a\sqrt{2}\hat{x}$, $\vec{a}_2 = a\hat{y}$ and $\vec{a}_3 = a\sqrt{2}\hat{z}$ along the $[\bar{1}10]$, $[001]$ and $[110]$ directions, respectively. The next step was to calculate, using DFT, the surface energy for these surfaces, using the following equation:

$$\text{Surface energy} = \frac{E_{\text{surf}} - E_{\text{bulk}}}{2A} \quad (1)$$

where E_{surf} is the energy of the β -TiNb001_Ti, β -TiNb001_Nb or β -TiNb(110) systems with surfaces, E_{bulk} is the β -TiNb energy for the same number and type of atoms and $2A$ is the area of the two surfaces existing in the system. The DFT surface energies are $0.798 \text{ eV}/\text{\AA}^2$ for the β -TiNb001_Ti, $0.826 \text{ eV}/\text{\AA}^2$ for the β -TiNb001_Nb and $0.186 \text{ eV}/\text{\AA}^2$ for the β -TiNb(110), revealing the (110) surface as energetically favoured in line with previous tight binding calculations for pure Nb [50].

Working on surfaces, another important feature is the contraction or expansion of the surface plane that is associated with the atomic plane difference normalized by the perfect bulk interatomic distance called the relative relax position (RR). We observed that

the surface layer of β -TiNb001_Ti, which consists of titanium atoms, has a contraction of -10.5% , while the second atomic plane of Nb atoms has an expansion of 2% . The third level of titanium atoms has an expansion of 6% , while the fourth level of Nb atoms shows complacency of -4% . The next atomic planes tend towards the bulk values. Similar behaviour is depicted for the β -TiNb001_Nb, where the contraction of the Nb surface plane is -9.5% . Both Ti- and Nb-terminated systems present similar RR values between the upper and bottom (001) surface layers. Turning on the β -TiNb(110) surface, we separately calculated RR for the Ti and Nb atoms of each mixed atomic plane, revealing a 2.5% expansion for the Ti surface atoms and -13% expansion for the Nb surface atoms, depicted with blue arrows in Figure 2a. The second layer Ti was contracted -7% while the corresponding Nb was expanded $+12\%$, leading to a zig-zag RR behaviour until the bulk values. The surface rippling effect is known for the alloy surfaces and has also been studied using molecular dynamics simulations for the case of Cu₃Au surfaces [51].

The β -TiNb(110) energetically favoured surface was chosen for further study. In Figure 2b, the electronic density of states projected on the surface atoms is presented. The valence band mainly occupies the range from -4 eV until the Fermi energy with a localized electron occupation at energies -2.5 eV and -1.0 eV. In addition, the presence of electrons at the Fermi reveals the metallic character of the material. The electron state density projected on the surface Ti and Nb atoms exhibits similar behaviour with a small altitude difference in the Fermi energy. These EDOS β -TiNb(001) behaviour is similar to the bulk β -TiNb EDOSs [49].

In Figure 2c, selective β -TiNb wavefunctions are presented. The WF at -30.33 eV is localized at the surface and in particular on Nb 4p surface atoms. It is worth noting the absolute lack of orbitals in the lower layers as well as the small overlap of the lobes of the atoms of the surface, which might lead to the possibility of forming bonds with active extra ions or molecules that might approach the surface at this energy level. In the top view projection on the (110) surface plane, it can be seen that the Ti surface 3p electrons also participate, while there is no visible directional bonding between the surface atoms. The Ti and Nb d electrons are depicted close to the Fermi energy in line with the EDOS of Figure 2b. At -0.01 eV, the Nb 4 d_{eg} and Ti 3 d_{eg} surface orbital form first neighbour in-plane directional hybridizations (highlighted by yellow dashed lines). Interestingly, the second- and third-layer atoms also participate in directional bonding along the [110]. Similar directional hybridizations vertical to the surface directional are shown at the WF $+0.09$ eV. The difference persists at the surface atoms, where the Nb 4d and Ti 3d orbital are bonded through two lobes with the second-layer atoms and not with the surface-layer atoms, leaving the other two lobes free, creating a type of dangling bonds at the surface.

Aiming to introduce antibacterial properties at the β -TiNb surface, the Ag atom and monolayer were considered and studied using DFT calculations. In Figure 3a, the main adsorption sites of Ag on β -TiNb(110) surface are presented along with the surface unit cell (dashed red rectangle). The first site is the one with Ag deposited over a second layer atom, known as the four-fold (FoF) position due to its quadruple symmetry. This position is herein named FoF_Ti or FoF_Nb site for the cases of Ti or Nb second-layer atom. Due to the periodically reproduced surface slab, the Ag deposition on FoF_Ti or FoF_Nb results in Ag surface semi-coverage, while when both sites are occupied by Ag atoms, they create full adlayer surface coverage. We also adsorb Ag on top of a Ti surface atom (we name this site OnTi) and on both Ti and Nb surface atoms (we named OnTiNb) not presented in this Figure. It should be noted that upon relaxation the OnTi and OnTiNb sites are not stable but the Ag adatom is relaxed towards the four-fold sites.

In all systems under study, contraction or expansion of the surface atoms was detected after Ag deposition. This phenomenon is called the expansion lattice strain effect and is common in metals. Surface expansion or contraction leads to the enhancement of the surface atoms–Ag interaction during adsorption, due to the greater Ag volume resulting in a deformation in the lattice structure close to the surface to integrate it as well as possible into the surface.

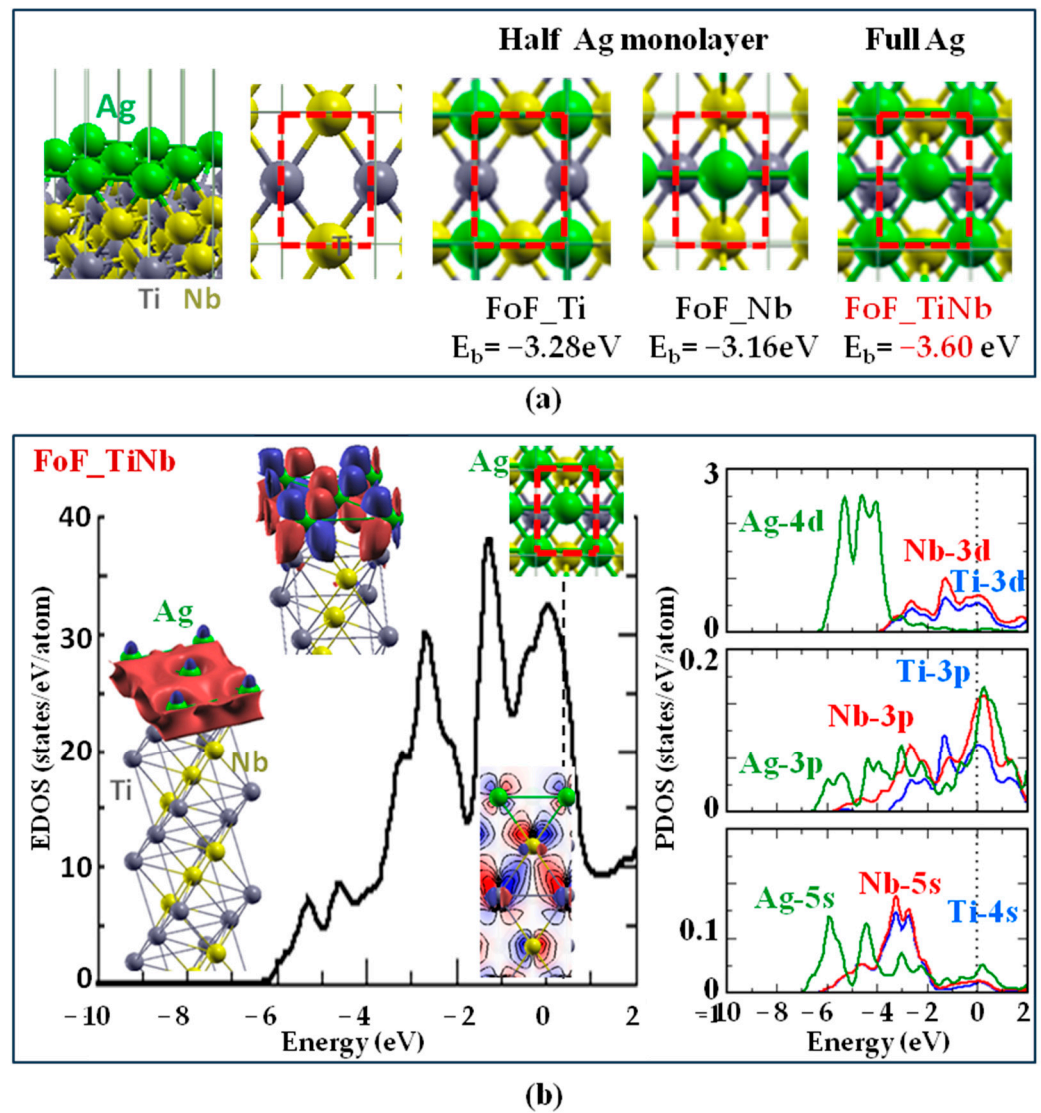


Figure 3. Ag 2D coating on β -TiNb(110) surface: (a) Schematic representation of Ag sites; (b) Ag, Ti and Nb partial electronic density of states along with characteristics wavefunctions at -6.7 eV, -2.22 eV and -0.11 eV. Fermi energy is at 0 eV. Grey, yellow and green spheres stand for Ti, Nb and Ag atoms. Red and blue charge areas stand for the positive and negative signs of the wavefunction (from -0.1 up to $+0.1$ $e^-/\text{\AA}^3$).

For all the above cases, the binding energy of Ag on the surface was calculated using the following equation:

$$E_{\text{bind}} = E_{\text{total}}^{\text{TiNbAg}} - \left(E^{\text{TiNb}} + E^{\text{Ag}} \right) \quad (2)$$

where $E_{\text{total}}^{\text{TiNbAg}}$ is the total energy of the system, E^{TiNb} is the total energy of the surface cell and E^{Ag} is the energy of the atom of the system. The Ag energetically favoured site is the FoF_Ti_Nb (-3.60 eV) followed by the FoF_Ti (-3.29 eV) and OnTi (-3.31 eV), FoF_Nb (-3.16 eV) and OnTiNb (-2.71 eV). Both Ti and Nb surface neighbouring atoms are contracted to Ag, while the Ag–Ti bond (2.73 \AA on average) is always shorter than Ag–Nb (2.85 \AA), although Nb surface atoms relax outwards. It should be noted that Ag from the initially ontop site relaxes towards the four-fold upon relaxation followed by the contraction of surface atoms. A possible expansion of the lattice could cause the d-band to shift to the Fermi energy, which in turn causes an amplification of the interaction of atoms deposited on the surface. The presence of Ag on β -TiNb affects the Ti surface atoms' relaxation (0.10 \AA) more than the Nb relaxation (0.02 \AA).

In Figure 3b, the electronic density of states for the Ag in the FoF_TiNb monolayer case is depicted along with characteristic wavefunctions. Similar to Ag in β -TiNb bulk in Figure 1, Ag introduces new energy states at lower energies than Ti and Nb. In particular, Ag 4d electron new energy states stand approximately from -6 eV up to -4 eV, mainly in the valence d-band, with two main peaks at -5.22 eV and -4.34 eV, altering the β -TiNb total EDOS. All atoms contribute in the energy range from -4 eV until the Fermi level with similar EDOS features. Due to the occupation at the Fermi energy, the system is metallic while the corresponding sharp peaks, where the d and p electrons mainly donate, denote structural instability. This is clearly visible in the p EDOS diagram, with a dominant peak of Nb 4p electrons appearing at the Fermi energy. The Ag-4p and Ti-3p at 0.18 eV and 0.22 eV, respectively, also contribute.

Similar behaviour is found in the EDOS diagrams of the Ag at FoF_Ti and FoF_Nb cases without such sharp occupancy in the Fermi energy. In the s-EDOS the Ag-5s exhibit two consecutive peaks at energy levels -5.87 eV and -4.38 eV, thus indicating their high occupation of states away from the Fermi energy, but also a sharp drop in the presence of electrons to -4.9 eV. Above the Fermi level, there is stronger occupation by Ti 3d and Nb 4d electrons, with a minimum of around $+1$ eV.

In the inset of Figure 3b, selective system wavefunctions are presented at -5.87 eV and -3.00 eV, where the occupation of the Ag electrons is dominant. Indeed, at -5.87 eV the Ag $4d_{eg}$ form directional bonds with the surface atoms while leaving the upper blue lobe free and active for further deposition. In addition, the parallel to the surface red part of the Ag $4d_{eg}$ orbital forms hybridizations between them, creating a strong electron plane where the Ag electrons exist. Turning on the WF at -3.00 eV, the Ag $4d_{t2g}$ orbitals are visible along with their directional hybridizations with the surface atoms, while two different sign lobes remain vertical to the surface pointing outwards, therefore creating active dangling-like bonds. In contrast, the WFs close to the Fermi level are homogeneously occupied by Ti 3d and Nb 4d electrons with a high possibility of directional hybridizations along the $[110]$ axes, while the Ag electrons are less filled or even show anti-bonding features with respect to the surface atoms (inset of WF pointing at the Fermi level).

Aiming to approach the solid solution features of the β -TiNb, we increased the size of the cell, creating a slab with 108 atoms, and randomly changed the positions of the Ti and Nb surface atoms, creating several configurations as presented in Figure 4a. In these systems, the two bottom layers were frozen in order to mimic the bulk β -TiNb system. All disorder cases having surface energy 0.174 eV/Å², 0.157 eV/Å², and 0.154 eV/Å² along with the segregated surface layer (0.156 eV/Å²) were energetically favoured compared to the perfect $\beta(110)$ configuration (0.186 eV/Å²) as presented by the calculated surface energy. Choosing the third disorder surface with 0.154 eV/Å², we adsorbed an Ag adatom on several sites. In Figure 4b, the Ag FoF_Ti is considered, having a binding energy of -4.21 eV, which is much lower than the periodic Ag monolayer of Figure 3.

It is found that the Ag adatom forms bonds with the four neighbouring surface atoms and more specifically with three niobium atoms and one titanium atom, stabilizing its adsorption. The distances between the atoms of Ag and the three atoms of Nb are 2.73 Å, 3.09 Å and 3.14 Å, while the Ag-Ti first neighbour distance is shorter at 2.70 Å. In addition, there is a contraction of the surface titanium by -0.007 Å. A Ag adatom was also deposited on a bridge site between Ti and Nb surface atoms, resulting in high binding energy of -4.05 eV. The Ag-Ti and Ag-Nb neighboring distances are 2.71 Å and 2.62 Å, respectively, being smaller than the corresponding FoF_Ti site. Furthermore, we placed the Ag atom over a Ti or Nb surface atoms named therefore OnTi and OnNb. The Ag-Ti first neighbor distance in the OnTi case is 2.51 Å while for the OnNb case the Ag-Nb bond is 2.58 Å. This result is in line with the smaller Ag binding energy of -3.51 eV of the OnTi against the -2.70 eV of the OnNb.

To conclude, the energetically favoured Ag adatom site is the FoF_Ti, which exhibits four Ag-surface atom bonds stabilizing this structure and making it less reactive against the other cases. For the cases where Ag ion detachment is needed, like in the implant

surfaces, the ideal site would be the OnNb with the weaker binding energy. Any other Ag site would offer a variety of cases that could serve a desired purpose.

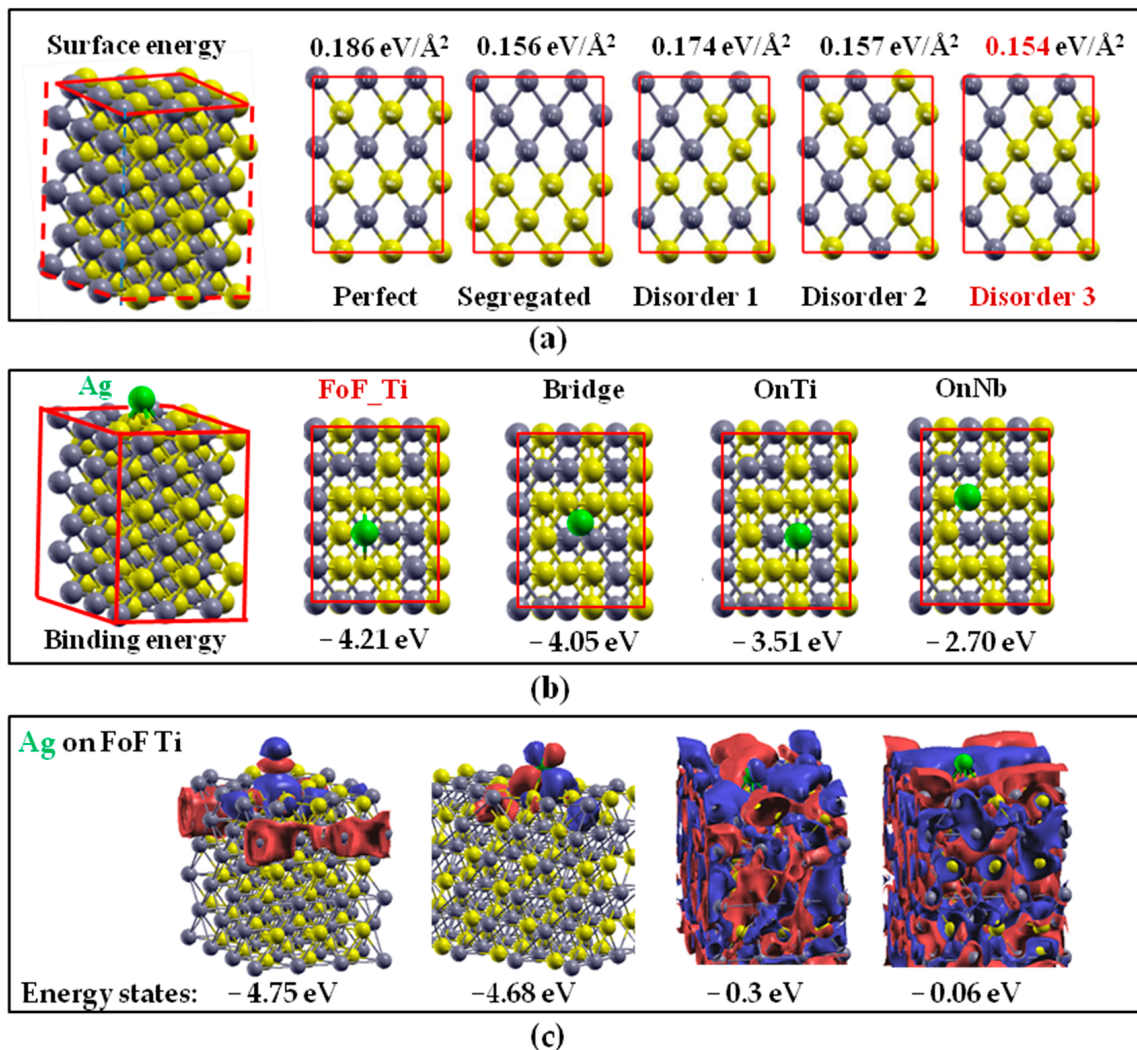


Figure 4. Ag adatom on β -TiNb(110). (a) Disorder β -TiNb(110) surfaces, (b) Ag adatom sites on the favoured disorder surface layer and (c) wavefunctions of Ag on the FoF_Ti position.

In Figure 4c, we present selective wavefunctions for the FoF_Ti site, energetically favoured by the Ag adatom. The WFs at -4.75 eV and -4.68 eV are due to the Ag 4d orbital and its surroundings. In particular, at -4.75 eV, the bottom blue lobe of the Ag 4d_{eg} orbital is bonded with the surface atoms, while the upper blue lobe is left free and active on the surface in case of further adatom or molecule adsorption. At -4.68 eV, two lobes with different signs (blue and red) of the Ag 4d_{t_{2g}} are unpaired, while the other two create directional hybridizations with the Nb first neighbouring surface atoms, stabilizing the Ag adatom position and creating an active site. In the energy states close to the Fermi level (-0.3 eV and -0.06 eV), WFs are distributed over the entire slab, offering several hybridizations between Ti–Nb and Ag atoms and creating sites suitable for further adsorption at the surface layer.

3.3. Ag Adsorption on TiO₂ Surfaces

Metal oxides are natively formed on the surfaces of the corresponding metallic diodes, introducing alteration in the structural and electronic properties of the substrate and therefore influencing the surface electron states, the Fermi level and the charge transfer. It is well known that TiO₂ mainly exhibits the rutile (thermodynamically stable) and anatase

phases. To this end, the Ag adsorption on the TiO₂ basic anatase and rutile surfaces was required. Initially, the electronic density of states, the electronic band gap along with the α and c lattice constants of both anatase and rutile were calculated (presented in the Supporting Information), in good agreement with previous experimental and theoretical data [52]. The presence of surfaces reduces the anatase and rutile band gap while surface states with even dangling bonds at the Fermi level might appear to enhance the ability for further metal or organic molecule adsorption. The detailed description of the surface atom projected electronic density along with available wavefunctions are presented in the Supporting Information. It should be noted that the presence of a surface in general narrows the TiO₂ bulk band gap due to the introduction of new surface states close to the Fermi level, especially in the cases of a titanium-rich terminated layer. These results are due to the well-known underestimation of the DFT band gap due to delocalization error [53,54].

Ag coating as half and full monolayer was considered on the oxygen-terminated anatase (001) and rutile (001) surfaces (the titanium-terminated surface exhibits rapid oxidation in the environment), similarly to the β -TiNb(110). The initial Ag half-monolayer adsorption sites are: (a) on top of the O-Ti outermost surface atoms (named OnOTi) and (b) the FoF (four-fold) position that are slightly altered upon relaxation. In the monolayer coating, both sites are occupied having the Ag–Ag distance equal to 2.86 Å. The Ag binding energy was calculated with the aim of revealing the energetically favoured deposition site that might create a stable and continued coating. For the case of metallic diodes, a well-bonded Ag film is desired for the alteration of the energy band gap and the protection of the titanium substrate from further oxidation, while for other applications, e.g., the creation of an antibacterial surface on an implant, the absence of metallic ions from the surface is preferred. The Ag binding energy was calculated for all three cases using the formula

$$E_{\text{binding}} = E_{\text{total}} - (E_{\text{surf}_{\text{TiO}_2}} + E_{\text{Ag}}) \quad (3)$$

where E_{total} is the minimum total energy of the TiO₂ surface in the presence of Ag, $E_{\text{surf}_{\text{TiO}_2}}$ is the energy of the pure surface O-terminated calculated in a previous section, and finally, E_{Ag} is the atomic energy of silver. Thus, for the half-monolayer on anatase (001), the silver binding energy of the OnOTi was calculated equal to -2.863 eV for the Ag FoF_O–Ti is equal to -0.7886 eV while for the monolayer coating is -3.09 eV or -1.55 eV/atom. According to these results, we conclude that the preferred position for the silver in the semi-coverage is the initial OnOTi surface atoms while the full monolayer coverage is the best one.

The total and partial electronic density of states of the Ag half-monolayer on oxygen-terminated TiO₂ anatase (001) at the initial OnOTi is depicted in Figure 5. In this PDOS diagram, the titanium atomic electronic states stand in blue lines, the oxygen atom ones in red lines and the silver in green lines. In Figure 5a, the lowest energy states around -18 eV are due to oxygen and silver. All atoms contribute to the broad valence band from -7 eV up to the Fermi level, while a clear Ag peak at the Fermi level introduces new states that narrow the band gap. The unoccupied states are mainly due to Ti 3d orbitals. The same features are shown in the d electron partial EDOS, where silver has a clear state at -17 eV and occupies the states close to the Fermi level. The Ti 3d orbitals contribute to the valence band from -7 eV up to Fermi and exhibit the highest unoccupied states. The p electron EDOS is mostly due to oxygen (revealing the highest peak at -18 eV) and to semi-core Ti 3p orbitals in the valence band close to the Fermi level. Similar behaviour is depicted for the s electron PDOS.

In the inset of Figure 5a, a wavefunction close to the Fermi level is presented. It should be noted that, although the Fermi level is found to be at -4.7786 eV, all states are shifted to $E_{\text{fermi}} = 0$ eV for comparison reasons. This wavefunction is due to the Ag atom and TiO₂ surface and substrate Ti and O atoms.

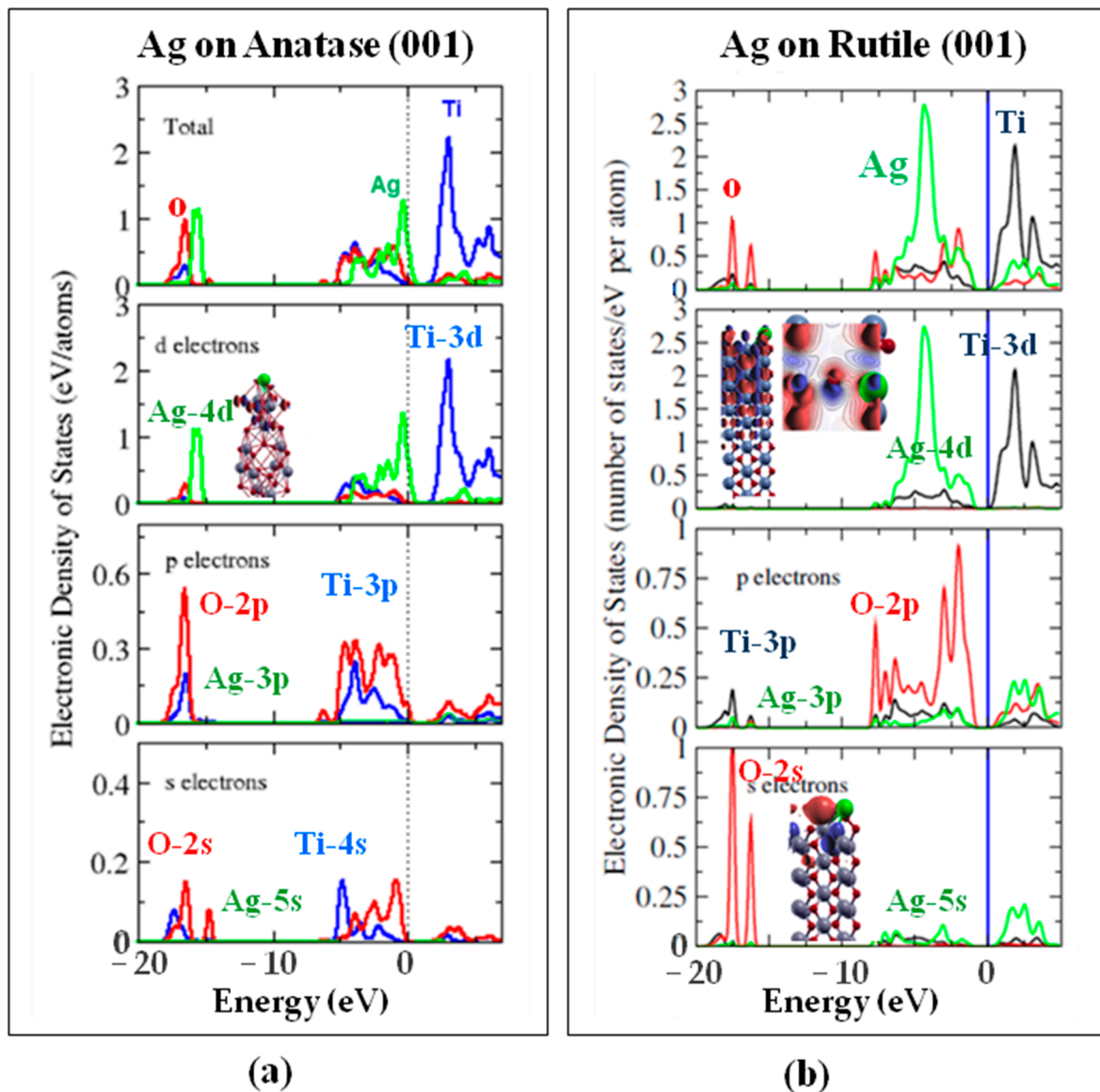


Figure 5. Electronic features of Ag 2D coat on (a) anatase (001) and (b) rutile (001) surfaces.

Silver deposition was also considered on the rutile (001) oxygen-terminated layer. Ag atoms were placed in similar sites as the the anatase cases: (a) half monolayer over O and Ti surface atoms (named OnOTi), (b) half monolayer on the four-fold (FoF) O–Ti site and (c) Ag monolayer in both positions. We started from the Ag OnOTi that is closer to the four-fold site than would be expected in a Ag fcc crystal. The bond distances between silver and its first neighbors are shown to vary from 2.4 Å (Ag–O) to 3.1 Å (Ag–Ti). The Ag–Ti bond distance is close to the c rutile lattice constant along [001] direction, while the Ag–O bond distances are similar (around 2.3 Å), suggesting the creation of an imaginary tetrahedron formed by Ag with its three neighbouring oxygen atoms. The Ag on the four-fold site is also shifted by approximately 0.5 Å upon relaxation. The Ag–Ti bond distance (3.654 Å) is higher than the ontop site, and the Ag–O neighbour bond distances are different (2.40 Å and 4.50 Å, respectively). In this case, no visible symmetry is observed between silver and oxygen atoms, while the relax site does not markedly affect the initial configuration. A silver rippled monolayer on rutile (001) is created when the Ag atoms occupy both previous sites. The initial and relax configurations are depicted to reveal the alteration in the structure of Ag deposition, which results in a difference in the vertically relaxed position and a rippled layer. In addition, due to the surface geometry, no further

visible Ag in-plane deposition site is available. The Ag initial sites are also altered, offering the Ag–Ti bond distances (3.1063 Å and 3.0303 Å) closer to the on-surface case, while the Ag–Ag bond distance (3.5434 Å) is the highest for this case. The Ag–O bond distances vary from 2.0198 Å to 3.0303 Å. The silver binding energy was calculated for all cases under study cases and found the OnOTi (−4.78 eV) as energetically favoured half-coverage site against the four-fold site (−4.68 eV) in line with the Ag deposition on anatase (001). The full rutile coverage is less favoured (−3.68 eV/atom). The Ag adsorption energies are in the energy range of previous ad initio calculations on TiO₂ (110) and CeO₂ (111) [33]. For the study of Ag rutile (001) surface electronic properties, the total state density (EDOS) diagrams for the titanium, oxygen and silver atoms as well as the partial state density diagrams (PDOS) of the s, p and d electrons of each atom were considered (Figure 5b). The EDOSs were normalized in such a way that the Fermi energy was set to zero in order to be comparable to each other and to previously discussed EDOSs. The first important observation is that the presence of silver clearly affects the rutile bulk and surface energy band gap. Silver introduces new states (mainly with Ag-4d character) into the energy gap where oxygen neighboring atoms participate. In the partial EDOS diagrams, a wide silver-occupied d-electron band from −7.5 eV to the Fermi level can be seen having a dominant electron peak around −4 eV for all three cases. In the d-orbital EDOSs, the Ti 3d and Ag 4d are occupying the valence band from −7.5 eV up to the Fermi level, revealing a major Ag 4d state around −5 eV and a Ti 3d unoccupied state around +1.5 eV. The p-electron PDOS is mainly due to oxygen atoms with a maximum peak close to the Fermi level at the highest occupied state. In contrast, the s-electron EDOS, due to oxygen, mainly occupies the states around −17 eV far from the Fermi level.

The study of the wavefunctions of the Ag-coated TiO₂ surfaces offers useful information for a better understanding of the created bonds and the coating stability. In the inset of Figure 5b, selective wavefunctions are depicted along with available hybridizations between silver and oxygen and/or titanium atoms. In the inset of s-electrons EDOS, the wavefunction corresponding to an energy $E = -16.1$ eV is depicted mainly due to oxygen s orbitals (red enhanced spheroid area), which form weak directional hybridizations with the Ag-3d_{eg} electrons (the d_{eg} electrons correspond to d_{z^2} or $d_{x^2-y^2}$ orbital that have their lobes along the z or x and y axis). In addition, the highest occupied wavefunction is presented in the inset of d-electron PDOS, where a high density of electrons is observed due to the surface oxygen 2p orbitals which form bonds with the Ag 3d_{eg} orbitals. Silver also has two unbonded 4d electron lobes located vertically to the surface layer that might be considered as dangly bonds, enhancing the surface activity.

In conclusion, Ag on both anatase and rutile (001) surfaces prefers the initial OnOTi sites and almost relaxes between the oxygen surface atoms with bonding hybridization close to the Fermi level, while the unbounded lobes create dangly bonds rendering this coating active for further adsorption.

4. Conclusions

In this work, the structural and electronic properties of β -TiNb and TiO₂ surfaces upon Ag deposition have been investigated. We found that Ag in β -TiNb prefers the Ti first neighbourhood in line with Ga, In and Sn cases, while introducing Ag 4d and Ag 5s localized electron states around −5 eV, altering the electronic properties of β -TiNb. The mix β -TiNb(110) surface is energetically favoured against the Ti- or O-terminated β -TiNb(001) surfaces exhibiting surface rippling with Ti surface atoms expanded by 2.5% and Nb surface atoms contracted −13%. Both Ti 3d and Nb 4d electrons contribute at the Fermi level with bonds between them and the substrate states, while states with dangly bond features at the Fermi level might help further adsorption. Localized surface states also exist at −30 eV from the Fermi level, which is shifted to 0.0 eV for comparison reasons. Ag adsorption on β -TiNb(110) smooths the surface atoms' rippling, exhibiting different relaxation sites with binding energy ranging from −2.70 eV up to −4.21 eV for the FoF_Ti site. In addition, Ag 4d electrons introduce electron states below −4 eV depending on the adsorption site,

which might form directional bonds with the surface atoms resulting in localization of the electron charge on the coating, while dangling bond states might appear at the Fermi level.

Aiming to approach the experimental observations of Ti-O passive film on the β -TiNb surfaces we further investigate the Ag adsorption on the basic TiO₂ anatase and rutile (001) faces. The presence of oxygen plays important role widening the β -TiNb electron states at the Fermi level introducing a band gap that is nevertheless smaller than the bulk TiO₂ anatase and rutile. This electronic band gap of TiO₂ is reduced when moving to surfaces, depending on the structure and chemistry in line with previous experimental and theoretical data. The calculated lattice constants and the bulk band gap of both anatase and rutile are in excellent agreement with the available experimental and theoretical data. Both in the Ti-O terminated anatase and rutile (001), surface states are introduced mainly due to the O 2p and Ti 3d electrons, especially at the Fermi level. A full or half Ag monolayer is bonded more strongly on rutile than anatase, offering a more stable antibacterial coating on this TiO₂ surface showing higher binding energy compare to the β -TiNb(110) surface. Ag 4d electron states are closer to the Fermi level than in the case of β -TiNb(110), while on anatase, they characterize the highest occupied states. For all cases, Ag 4d electrons affect the electron states from -5 eV up to the Fermi level depending on the coating and surface structure as well as the type of neighbouring surface atoms (Ti, O or Nb), offering a variety of different cases that could be used for the design of thin film semiconductors with a tunable electron band gap.

Supplementary Materials: The following supporting information can be downloaded at <https://www.mdpi.com/article/10.3390/cryst14050428/s1>, Figure S1: Electronic features of TiO₂ anatase and oxygen and Ti-O-terminated anatase (001) surfaces along with selective wavefunctions; Figure S2: Electronic features of TiO₂ rutile and rutile (001) surface. Refs. [52–54] are cited in this part.

Author Contributions: S.P.-C.: formal analysis; A.C.G.: formal analysis; D.F.: formal analysis; C.K.: formal analysis; A.M.: formal analysis; M.E.N.: formal analysis; T.A.: project administration and funding acquisition; E.L.: writing—review and editing; C.E.L.: supervision, writing—original draft preparation—review and editing. All authors have read and agreed to the published version of the manuscript.

Funding: This research was funded by the Bioremia Project (H2020-MSCA-ITN-2019, No 861046, 2020–2024) and by the LASEMAL Project (King Abdullah University of Science and Technology (KAUST)) Office of Sponsored Research (OSR) under Award No: OSR-2020-CRG9-4347).

Data Availability Statement: The original contributions presented in the study are included in the article/Supplementary Material, further inquiries can be directed to the corresponding author.

Acknowledgments: This work is supported by the Bioremia Project (H2020-MSCA-ITN-2019, No 861046, 2020–2024) and by the LASEMAL Project (King Abdullah University of Science and Technology (KAUST)) Office of Sponsored Research (OSR) under Award No: OSR-2020-CRG9-4347.

Conflicts of Interest: The authors declare no conflict of interest.

References

1. Greer, A.L. Metallic glasses. . . on the threshold. *Mater. Today* **2009**, *12*, 14. [[CrossRef](#)]
2. Padmanabhan, J.; Kinsler, E.R.; Stalter, M.A.; Duncan-Lewis, C.; Balestrini, J.L.; Sawyer, A.J.; Schroers, J.; Kyriakides, T.R. Engineering Cellular Response Using Nanopatterned Bulk Metallic Glass. *ACS Nano* **2014**, *8*, 4366. [[CrossRef](#)] [[PubMed](#)]
3. Shah, F.A.; Thomsen, P.; Palmquist, A. Osseointegration and current interpretations of the bone-implant interface. *Acta Biomater.* **2019**, *84*, 1–15. [[CrossRef](#)] [[PubMed](#)]
4. Alonzo, M.; Primo, F.A.; Kumar, S.A.; Mudloff, J.A.; Dominguez, F.; Fregoso, G.; Ortiz, A.; Weiss, W.M.; Joddar, B. Bone tissue engineering techniques, advances, and scaffolds for treatment of bone defects. *Curr. Opin. Biomed. Eng.* **2021**, *17*, 100248. [[CrossRef](#)] [[PubMed](#)]
5. Sun, K.; Fu, R.; Liu, X.W.; Xu, L.M.; Wang, G.; Chen, S.Y.; Zhai, Q.J.; Pauly, S. Osteogenesis and angiogenesis of a bulk metallic glass for biomedical implants. *Bioact. Mater.* **2022**, *8*, 253–266. [[CrossRef](#)] [[PubMed](#)]
6. Calin, M.; Helth, A.; Gutierrez Moreno, J.J.; Bönisch, M.; Brackmann, V.; Giebler, L.; Gemming, T.; Lekka, C.E.; Gebert, A.; Schnettler, R.; et al. Elasticsofteningofbeta-typeTi-Nballoysby(In)additions. *J. Mech. Behav. Biomed. Mater.* **2014**, *39*, 162.

7. Kauschke, V.; Gebert, A.; Calin, M.; Eckert, J.; Scheich, S.; Heiss, C.; Lips, K.S. Effects of new beta-type Ti-40Nb implant materials, brain-derived neurotrophic factor, acetylcholine and nicotine on human mesenchymal stem cells of osteoporotic and non osteoporotic donors. *PLoS ONE* **2018**, *13*, e0193468. [[CrossRef](#)] [[PubMed](#)]
8. Piszczek, P.; Kubiak, B.; Golińska, P.; Radtke, A. Oxo-Titanium(IV) Complex/Polymer Composites—Synthesis, Spectroscopic Characterization and Antimicrobial Activity Test. *Int. J. Mol. Sci.* **2020**, *21*, 9663. [[CrossRef](#)] [[PubMed](#)]
9. Yu, X.; Marks, T.J.; Facchetti, A. Metal Oxides for Optoelectronic Applications. *Nat. Mater.* **2016**, *15*, 383–396. [[CrossRef](#)]
10. Nomura, K.; Ohta, H.; Ueda, K.; Kamiya, T.; Hirano, M.; Hosono, H. Thin-Film Transistor Fabricated in Single-Crystalline Transparent Oxide Semiconductor. *Science* **2003**, *300*, 1269–1272. [[CrossRef](#)]
11. Petti, L.; Münzenrieder, N.; Vogt, C.; Faber, H.; Büthe, L.; Cantarella, G.; Bottacchi, F.; Anthopoulos, T.D.; Tröster, G. Metal Oxide Semiconductor Thin-Film Transistors for Flexible Electronics. *Appl. Phys. Rev.* **2016**, *3*, 021303. [[CrossRef](#)]
12. Yarali, E.; Koutsiki, C.; Faber, H.; Tetzner, K.; Yengel, E.; Patsalas, P.; Kalfagiannis, N.; Koutsogeorgis, D.C.; Anthopoulos, T.D. Recent Progress in Photonic Processing of Metal-Oxide Transistors. *Adv. Funct. Mater.* **2020**, *30*, 1906022. [[CrossRef](#)]
13. Bouri, M.; Lekka, C.E. L-Glutamine Coating on Antibacterial Cu Surface by Density Functional Theory. *Crystals* **2023**, *13*, 1698. [[CrossRef](#)]
14. Xu, L.C.; Siedlecki, C.A. Antibacterial Polyurethanes. *Adv. Polyurethane Biomater.* **2016**, 247–284. [[CrossRef](#)]
15. Rossos, A.K.; Banti, C.N.; Raptis, P.K.; Papachristodoulou, C.; Sainis, I.; Zoumpoulakis, P.; Mavromoustakos, T.; Hadjikakou, S.K. Silver Nanoparticles Using Eucalyptus or Willow Extracts (AgNPs) as Contact Lens Hydrogel Components to Reduce the Risk of Microbial Infection. *Molecules* **2021**, *26*, 5022. [[CrossRef](#)] [[PubMed](#)]
16. Ahmad, S.A.; Das, S.S.; Khatoun, A.; Ansari, M.T.; Afzal, M.; Saquib Hasnain, M.; Nayak, A.K. Bactericidal activity of silver nanoparticles: A mechanistic review. *Mater. Sci. Energy Technol.* **2020**, *3*, 756–769. [[CrossRef](#)]
17. Naik, A.; Best, S.; Cameron, R. Influence of silanisation on the mechanical and degradation behaviour of PLGA/HA composites. *Mater. Sci. Eng. C* **2015**, *48*, 642. [[CrossRef](#)]
18. Vijayan, V.; Kiran, M.S. Hybrid nanostructured gadolinium oxide collagen-dextran polymeric hydrogel for corneal repair and regeneration. *Int. J. Biol. Macromol.* **2023**, *224*, 1423–1438. [[CrossRef](#)]
19. Alberta, L.A.; Vishnu, J.; Hariharan, A.; Pilz, S.; Gebert, A.; Calin, M. Novel low modulus beta-type TiNb alloys by gallium and copper minor additions for antibacterial implant applications. *J. Mater. Res. Technol.* **2022**, *20*, 3306. [[CrossRef](#)]
20. Akman, A.; Alberta, L.A.; Giraldo-Osorno, P.L.; Turner, A.B.; Hantusch, M.; Palmquist, A.; Trobos, M.; Calin, M.; Gebert, A. Effect of minor gallium addition on corrosion, passivity, and antibacterial behaviour of novel b-type Ti-Nb alloys. *J. Mater. Res. Technol.* **2023**, *25*, 4110. [[CrossRef](#)]
21. Alberta, L.A.; Fortouna, Y.; Vishnu, J.; Pilz, S.; Gebert, A.; Lekka, C.E.; Nielsch, K.; Calin, M. Effects of Ga on the structural, mechanical and electronic properties of β -Ti45Nb alloy by experiments and ab initio calculations. *J. Mech. Behav. Biomed. Mater.* **2023**, *140*, 105728. [[CrossRef](#)] [[PubMed](#)]
22. Liu, S.; Zhang, Z.; Zhang, J.; Qin, G.; Zhang, E. Construction of a TiO₂/Cu₂O multifunctional coating on Ti-Cu alloy and its influence on the cell compatibility and antibacterial properties. *Surf. Coat. Technol.* **2021**, *421*, 127438. [[CrossRef](#)]
23. Zhang, L.; Guo, J.; Huang, X.; Zhang, Y.; Han, Y. The dual function of Cu-doped TiO₂ coatings on titanium for application in percutaneous implants. *J. Mater. Chem. B* **2016**, *4*, 3788. [[CrossRef](#)]
24. Fornell, J.; Soriano, J.; Guerrero, M.; Sirvent, J.D.D.; Ferran-Marqués, M.; Ibáñez, E.; Barrios, L.; Baró, M.D.; Suriñach, S.; Nogués, C.; et al. Biodegradable FeMnSi Sputter-Coated Macroporous Polypropylene Membranes for the Sustained Release of Drugs. *Nanomaterials* **2017**, *7*, 155. [[CrossRef](#)] [[PubMed](#)]
25. Bartkowska, A.; Lekka, C.E.; Alberta, L.A.; Spasojevic, I.; Pellicer, E.; Sort, J. Silver-induced $\gamma \rightarrow \epsilon$ martensitic transformation in FeMn alloys: An experimental and computational study. *J. Alloys Compd.* **2023**, *966*, 171640. [[CrossRef](#)]
26. Pawar, T.J.; Lopez, D.C.; Olivares Romero, J.L.; Montesinos, J.V. Surface modification of titanium dioxide. *J. Mater. Sci.* **2023**, *58*, 6887–6930. [[CrossRef](#)]
27. Durango-Giraldo, G.; Cardona, A.; Zapata, J.F.; Santa, J.F.; Buitrago-Sierra, R. Titanium dioxide modified with silver by two methods for bactericidal applications. *Heliyon* **2019**, *5*, 01608. [[CrossRef](#)] [[PubMed](#)]
28. Vallejo-Montesinos, J.; Gámez-Cordero, J.; Zarraga, R.; Pérez Pérez, M.C.; Gonzalez-Calderon, J.A. Influence of the surface modification of titanium dioxide nanoparticles TiO₂ under efficiency of silver nanodots deposition and its effect under the properties of starch–chitosan (SC) films. *Polym. Bull.* **2020**, *77*, 107–133. [[CrossRef](#)]
29. Gao, A.; Hang, R.; Huang, X.; Zhao, L.; Zhang, X.; Wang, L.; Tang, B.; Ma, S.; Chu, P.K. The effects of titania nanotubes with embedded silver oxide nanoparticles on bacteria and osteoblasts. *Biomaterials* **2014**, *35*, 4223–4235. [[CrossRef](#)]
30. Zhang, P.; Zhang, Z.; Li, W. Antibacterial TiO₂ Coating Incorporating Silver Nanoparticles by Microarc Oxidation and Ion Implantation. *J. Nanomater.* **2013**, *2013*, 542878.
31. Quiñones-Jurado, Z.V.; Waldo-Mendoza, M.A.; Aguilera-Bandin, H.M.; Villabona-Leal, E.G.; Cervantes-González, E.; Pérez, E. Silver Nanoparticles Supported on TiO₂ and Their Antibacterial Properties: Effect of Surface Confinement and Nonexistence of Plasmon Resonance. *Mater. Sci. Appl.* **2014**, *5*, 895–903.
32. Skiba, M.; Vorobyova, V.; Pasenko, O. Surface modification of titanium dioxide with silver nanoparticles for application in photocatalysis. *Appl. Nanosci.* **2022**, *12*, 1175–1182. [[CrossRef](#)]
33. O'Connor, N.J.; Jonayat, A.S.M.; Janik, M.J.; Senftle, T.P. Interaction trends between single metal atoms and oxide supports identified with density functional theory and statistical learning. *Nat. Catal.* **2018**, *1*, 531–539. [[CrossRef](#)]

34. Branda, M.M.; Hernandez, N.C.; Sanz, J.F.; Illas, F. Density functional theory study of the interaction of Cu, Ag, and Au atoms with the regular CeO₂(111) surface. *J. Phys. Chem. C* **2010**, *114*, 1934–1941. [[CrossRef](#)]
35. Giordano, L.; Baistrocchi, M.; Pacchioni, G. Bonding of Pd, Ag, and Au atoms on MgO(100) surfaces and MgO/Mo(100) ultra-thin films: A comparative DFT study. *Phys. Rev. B* **2005**, *72*, 11. [[CrossRef](#)]
36. Kresse, G.; Furthmüller, J. Efficiency of ab-initio total energy calculations for metals and semiconductors using a plane-wave basis set. *Comput. Mater. Sci.* **1996**, *6*, 15–50. [[CrossRef](#)]
37. Kresse, G.; Furthmüller, J. Efficient iterative schemes for ab initio total-energy calculations using a plane-wave basis set. *Phys. Rev. B* **1996**, *54*, 11169–11186. [[CrossRef](#)] [[PubMed](#)]
38. Sanchez-Portal, D.; Ordejon, P.; Artacho, E.; Soler, J.M. Density-Functional Method for Very Large Systems with LCAO Basis Sets. *Int. J. Quantum Chem.* **1997**, *65*, 453–461. [[CrossRef](#)]
39. Artacho, E.; Sanchez-Portal, D.; Ordejon, P.; Garcia, A.; Soler, J.M. Linear-Scaling ab-Initio Calculations for Large and Complex Systems. *Phys. Status Solidi B* **1999**, *215*, 809–817. [[CrossRef](#)]
40. Perdew, J.P.; Burke, K.; Ernzerhof, M. Generalized Gradient Approximation Made Simple. *Phys. Rev. Lett.* **1996**, *77*, 3865–3868. [[CrossRef](#)]
41. Kresse, I.G.; Joubert, D. From ultrasoft pseudopotentials to the projector augmented-wave method. *Phys. Rev. B* **1999**, *59*, 1758. [[CrossRef](#)]
42. Blöchl, P.E. Projector augmented-wave method. *Phys. Rev. B* **1994**, *50*, 17953. [[CrossRef](#)] [[PubMed](#)]
43. Rangarajan, S.; Mavrikakis, M. A comparative analysis of different van der Waals treatments for molecular adsorption on the basal plane of 2H-MoS₂. *Surf. Sci.* **2023**, *729*, 122226. [[CrossRef](#)]
44. Grimme, S.; Antony, A.; Ehrlich, S.; Krieg, H. A consistent and accurate ab initio parametrization of density functional dispersion correction (DFT-D) for the 94 elements H-Pu. *J. Chem. Phys.* **2010**, *132*, 154104. [[CrossRef](#)]
45. Araujo, R.B.; Rodrigues, G.L.S.; Campos dos Santos, E.; Pettersson, L.G.M. Adsorption energies on transition metal surfaces: Towards an accurate and balanced description. *Nat. Commun.* **2022**, *13*, 6853. [[CrossRef](#)] [[PubMed](#)]
46. Gutiérrez Moreno, J.J.; Papageorgiou, D.G.; Evangelakis, G.A.; Lekka, C.E. An ab initio study of the structural and mechanical properties of Ti-Nb alloys. *J. Appl. Phys.* **2018**, *124*, 245102. [[CrossRef](#)]
47. Gutiérrez Moreno, J.J.; Panagiotopoulos, N.T.; Evangelakis, G.A.; Lekka, C.E. Electronic Origin of α'' to β Phase Transformation in Ti-Nb-Based Thin Films upon Hf Microalloying. *Materials* **2020**, *13*, 1288. [[CrossRef](#)] [[PubMed](#)]
48. Jiang, X.; Zhao, J.; Jiang, X. Correlation between hardness and elastic moduli of the covalent crystals. *Comput. Mater. Sci.* **2011**, *50*, 2287–2290. [[CrossRef](#)]
49. Lekka, C.E.; Gutiérrez-Moreno, J.J.; Calin, M. Electronic origin and structural instabilities of Ti-based alloys suitable for orthopaedic implants. *J. Phys. Chem. Solids* **2017**, *102*, 49. [[CrossRef](#)]
50. Lekka, C.E.; Mehl, M.J.; Bernstein, N.; Papaconstantopoulos, D.A. Tight binding molecular dynamics simulations of Nb surfaces and surface defects. *Phys. Rev. B* **2003**, *68*, 35422. [[CrossRef](#)]
51. Lekka, C.E.; Papanicolaou, N.I.; Evangelakis, G.A. Molecular dynamics study of the ordered Cu₃Au. I Vibrational and structural properties of the low-indexed Cu₃Au surfaces by Molecular Dynamics Simulations. *Surf. Sci.* **2001**, *479*, 287. [[CrossRef](#)]
52. Prasai, B.; Cai, B.; Underwood, M.K.; Lewis, J.P.; Drabold, D.A. Properties of amorphous and crystalline titanium dioxide from first principles. *J. Mater. Sci.* **2012**, *47*, 7515–7521. [[CrossRef](#)]
53. Perdew, J.P. Density functional theory and the band gap problem. *Int. J. Quantum Chem. Quantum Chem. Symp.* **1986**, *19*, 497–523. [[CrossRef](#)]
54. Fahrenkamp-Uppenbrink, J.; Szuromi, P.; Veston, J.; Coontz, R. Theoretical Possibilities. *Science* **2008**, *321*, 794. [[CrossRef](#)] [[PubMed](#)]

Disclaimer/Publisher’s Note: The statements, opinions and data contained in all publications are solely those of the individual author(s) and contributor(s) and not of MDPI and/or the editor(s). MDPI and/or the editor(s) disclaim responsibility for any injury to people or property resulting from any ideas, methods, instructions or products referred to in the content.